Weakly Supervised Inversion of Multi-physics Data for Geophysical Properties

Anonymous Authors[1]

Abstract

Multi-physics inversion plays a critical role in geophysics. It has been widely used to simultaneously infer various geophysical properties (such as velocity and conductivity). Among those inversion problems, some are explicitly governed by partial differential equations (PDEs), while others are not. Without explicit governing equations, conventional physical-based inversion techniques are not feasible and data-driven inversion requires expensive full labels. To overcome this issue, we proposed a new data-driven multi-physics inversion technique with extremely weak supervision. Our key finding is that the pseudo labels can be constructed by learning the local relationship among geophysical properties at very sparse locations. We explore the multi-physics inversion problem from two distinct measurements (seismic and electromagnetic data) to three geophysical properties (velocity, conductivity, and CO_2 saturation) with synthetic data based on the Kimberlina storage reservoir in California. Our results show that we are able to invert for properties without explicit governing equations. Moreover, the label data on three geophysical properties can be significantly reduced by 50 times (from 100 down to only 2 locations).

1. Introduction

Geophysical properties (such as velocity, conductivity and CO_2 saturation) provide structural and numerical information for various geophysical applications, e.g. assessment of oil and gas reservoirs and sequestration of CO_2 (Lucia et al., 2003). These properties are obtained from surface-based geophysical measurements including seismic (Yilmaz, 2001), electromagnetics (EM) (Zhdanov, 2009), gravity (Li & Oldenburg, 1998), etc, by geophysical inversion. .

[1]Anonymous Institution, Anonymous City, Anonymous Region, Anonymous Country. Correspondence to: Anonymous Author <anon.email@domain.com>.

Preliminary work. Under review by the International Conference on Machine Learning (ICML). Do not distribute.

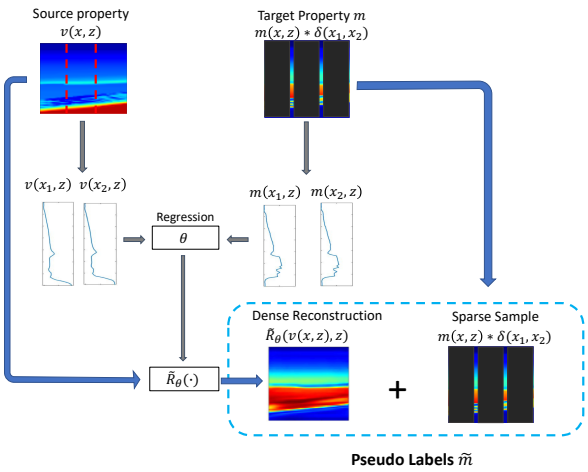

Figure 1. Schematic illustration of our proposed method, which generate the pseudo labels $\tilde{m}$ from the sparse sampling of the target property m and the full labeling of the source property v.

These inversion problems have been studied *separately* (see Fig. 2) along two directions: physics-driven and data-driven. The physics-driven methods (Zhdanov et al., 2000; Virieux & Operto, 2009; Feng & Schuster, 2019; Chen et al., 2020; Feng et al., 2021a) are applicable for seismic→velocity and EM→conductivity by leveraging the known PDE, which is converted as a forward modeling operator such that the input (seismic or EM) is a function of output (velocity or conductivity). Based on the forward modeling, velocity and conductivity can be iteratively optimized. The data-driven methods apply to the inversion problems by leveraging deep neural networks to learn a correspondence from geophysical measurements to geophysical properties (Araya-Polo et al., 2018; Wu & Lin, 2019; Feng et al., 2021b). This type of works requires a large amount of paired geophysical measurements and geophysical properties to train the network.

The information from different geophysical methods is usually mutually complementary. Jointly inverting multiple geophysical data simultaneously collected from the same area can improve the estimation of geophysical properties and reduce the uncertainty (Zhdanov et al., 2021). Joint multi-physics inversion has been widely studied among

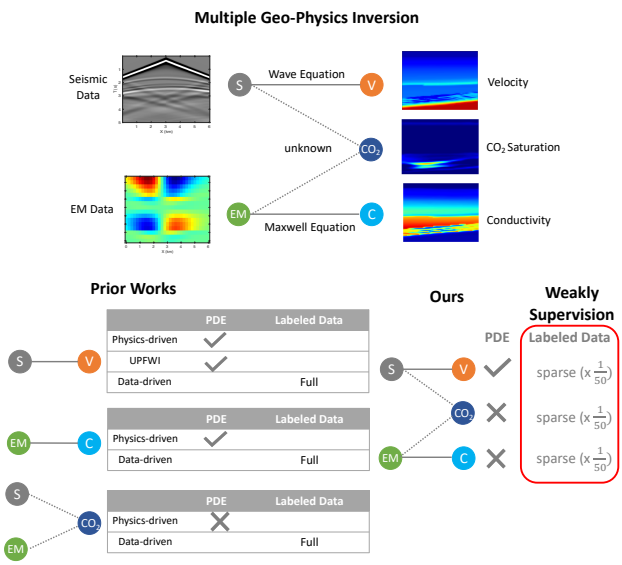

Figure 2. Schematic illustration of the Weakly Supervised Multiple Geo-Physics Inversion (WS-MGI) and the comparison with the prior works. The prior works are mainly achieved by physics-driven and data-driven methods. The physics-driven methods can invert the geophysical properties governed by PDEs, such as velocity and conductivity (governed by wave and Maxwell equations). The data-driven methods require fully-labeled data for network training

the physics-driven methods with the properties explicitly governed by the PDEs (such as velocity and conductivity) (Hoversten et al., 2003; Lelièvre et al., 2012). But the physics-driven methods are unable to invert properties without explicit governing equations (such as CO_2 saturation) since the gradient in the iterative optimization can not be solved.

Supervised data-driven methods can obtain properties without explicit governing equations. Sun et al. (2020) presented a joint inversion that reconstructs salt geometry by combining seismic and electromagnetic data, it still relies on a large amount of labeled data. However, the acquisition of the labeled data is extremely expensive, only sparse labeled data can be acquired in the field experiments.

In this work, we shift the data-driven inversion paradigm to *jointly* address these three inversion problems with *extremely weak* supervision (see Fig. 2). The three inversion problems are as follows: (a) seismic→velocity to recover velocity maps from seismic data, (b) EM→conductivity to recover conductivity maps from EM data, and (c) seismic/EM→CO_2 to recover CO_2 saturation maps from seismic and EM data. The first two are governed by PDEs (wave and Maxwell's equation), while the physics for the last one is unknown. Only $\frac{1}{50}$ samples in the maps are labeled. We propose a two-stage solution for these problems. In the first step, a single-physics inversion is performed in an unsupervised way. In the second step, we construct the pseudo labels by approximating the relationship between the geophysical properties, which enable the inversion of the properties that do not have explicit governing equations. The requirement of the multi-physics labeled data is greatly reduced. We name our multi-physics method Weakly Supervised Multiple Geo-Physics Inversion (WS-MGI) and evaluate our methodology on the Kimberlina reservoir data (Alumbaugh et al., 2021). These numerical results demonstrate that WS-MGI can accurately reconstruct the subsurface structures with sparsely labeled data.

2. Backgrounds and Related Works

A geophysical survey collects the multi-physics data to extract useful information about the geophysical properties. Geophysical forward modeling can be formulated as

$$\mathbf{d} = f(\mathbf{m}), \tag{1}$$

where $\mathbf{d}$ is the geophysical measurement, $\mathbf{m}$ is the geophysical properties and f is the geophysical forward modeling operator.

Some of the forward modeling operator f is governed by the PDEs. For example, the velocity maps and seismic measurements are correlated through the acoustic-wave equation as follows (Schuster, 2017):

$$\nabla^2 p(\mathbf{r}, t) - \frac{1}{v^2(\mathbf{r})} \frac{\partial^2 p(\mathbf{r}, t)}{\partial t^2} = s(\mathbf{r}, t), \tag{2}$$

where $v(\mathbf{r})$ is the velocity at spatial location $\mathbf{r}$, $\nabla^2 = \left(\frac{\partial^2}{\partial x^2} + \frac{\partial^2}{\partial z^2}\right)$ is the Laplacian operator in 2D Cartesian coordinates, $s(\mathbf{r}, t)$ is the source term, $p(\mathbf{r}, t)$ is the pressure data, and t represents time.

Similarly, the conductivity map and EM measurements are correlated through the Maxwell's equations as follows (Commer & Newman, 2008):

$$\begin{aligned} \sigma \mathbf{E} - \nabla \times \mathbf{H} &= -\mathbf{J}, \\ \nabla \times \mathbf{E} + i\omega\mu_0 \mathbf{H} &= -\mathbf{M}, \end{aligned} \tag{3}$$

where $\mathbf{H}$ and $\mathbf{E}$ are the magnetic and electric fields, respectively. $\mathbf{J}$ and $\mathbf{M}$ are the electric and magnetic sources. σ is the electrical conductivity and μ_0 is the magnetic permeability of free space that $\mu_0 = 4\pi \times 10^{-7}$ ohm-seconds per meter.

Given the forward modeling operator f, the physics-driven method invert the geophysical properties $\mathbf{m}$ by minimizing

the loss function:

$$\mathcal{L}_{\text{geo}} = \frac{1}{2}||f(\mathbf{m}) - \mathbf{d}||^2. \tag{4}$$

where $\mathbf{d}$ is the geophysical measurement.

However, some geophysical properties, such as CO_2 saturation, are not connected to the surface-based geophysical measurements by PDEs and f is unknown. The physics-driven methods are not feasible for such properties (see Fig. 2).

In the data-driven methods, convolutional neural networks $g(\cdot)$ are trained to approximate the inverse mapping $f^{-1}(\cdot)$ from geophysical measurement $\mathbf{d}$ to geophysical properties $\mathbf{m}$ whether f is known:

$$\mathbf{m} = g(\mathbf{d}) \approx f^{-1}(\mathbf{d}). \tag{5}$$

Such methods are able to invert all the geophysical properties with the requirement of paired geophysical measurement $\mathbf{d}$ and labeled geophysical properties $\mathbf{m}$ for the training.

The accurate labeled geophysical properties can only be obtained from well logs, which are collected by the instruments lowered in a borehole that is penetrating the geologic formations (Ellis & Singer, 2007). The borehole is drilled vertically aiming at a target directly below the surface (Ma et al., 2016). The drilling is very expensive and only a few boreholes are drilled in the field experiments (Bassiouni et al., 1994; Lukawski et al., 2014), so the labeled properties are always sparse.

Pseudo Labels in Computer Vision vs. Geophysics

In this paper, we have used pseudo labels to enable the multi-physics data-driven inversion of properties and overcome the sparse sampling problem in geophysics. Notice that there are differences between the pseudo labels in our problems and those in Computer Vision.

Pseudo labels are used in semi-supervised learning in the Computer Vision area (Lee et al., 2013). The network is initially trained with a small set of labeled data. Then the confidently predicted test data is added to the training data as the pseudo label to fine-tune the network. The building of the pseudo labels is based on the information from the same type of momentum.

In our methods with geophysics, the building of pseudo labels is based on its relationships with the other geophysical properties, which are the other types of momentum. Moreover, there are no existing small labeled data sets for the initial training. Only sparse labeled data are available.

3. Methods

Multiple Geo-physics Inversion of the properties (such as CO_2 saturation) without explicit governing equations can only be achieved by supervised data-driven methods in the previous works. These methods are not feasible in real cases since the collection of the labeled data is too expensive. Only sparse labeled data are available in the field, a weakly supervised data-driven inversion method is required for solving the multi-physics inversion.

3.1. Weakly Supervised Multiple Geo-physics Inversion

Here we proposed a Weakly Supervised Multiple Geo-physics Inversion (WS-MGI) method to invert multi-physics properties (source property v and target property m) with sparse samples. The samples are well logs $m(x = x_k, z)$, where x_k is the drilling location. The source property v is a property related to the geophysical measurements with PDEs while the target property m is the property without explicit governing equations. WS-MGI is implemented in two stages:

Stage 1: Invert for source property v from the geophysical measurements using an unsupervised method.

Stage 2: With the sparse sampling of target property $m(x = x_k, z)$ and the inverted source property at the corresponding location $v(x = x_k, z)$, we generate the pseudo labels $\tilde{m}$ and train an end-to-end network with $\tilde{m}$ to learn the mapping from geophysical measurement to m (Fig. 3). The trained network is then applied to the measurement to invert m.

3.2. Two-stage Solution

Stage 1. Unsupervised Single Geophysical Inversion: Stage 1 is an unsupervised inversion for single geophysical property v, which had already been proposed by Jin et al. (2021) as Unsupervised Physical-Informed Full Waveform Inversion (UPFWI) for velocity maps as v. However, the unsupervised learning methods are still unavailable for other geophysical properties, such as conductivity and CO_2 saturation. UPFWI connects the PDE and neural network to obtain the velocity map in an unsupervised way. The details of the UPFWI are given in the Appendix.

Stage 2. Pseudo Labels Building and Training: To build the pseudo labels in Stage 2, we construct a simple regression model $\tilde{R}$ using support vector regression (SVR) with a Gaussian Kernel. The sparse sample $m(x = x_k, z)$ and v at its corresponding location $v(x = x_k, z)$ are discretized into N training samples:

$$\left(\begin{pmatrix} v^{(i)} \\ z^{(i)} \end{pmatrix}, m^{(i)} \right), \tag{6}$$

where $i = 1, 2, ..., N$. The model $\tilde{R}_\theta(\cdot)$ is trained by mini-

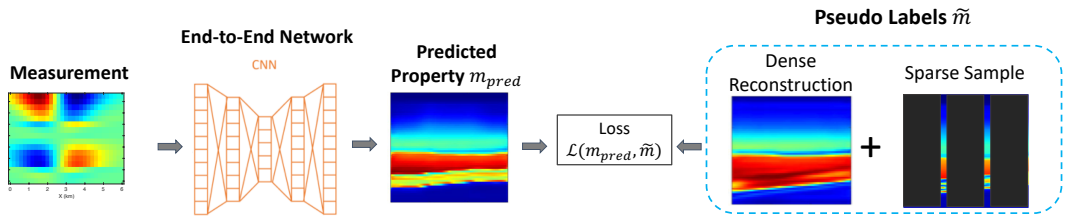

Figure 3. Schematic illustration of the encoder-decoder trained with the pseudo labels. The pseudo labels that consist of dense reconstructions and sparse samples are used in the loss function to train a end-to-end network for the prediction of geophysical properties.

mizing

$$\sum_{N} \left\{ \tilde{R}_\theta(v^{(i)}, z^{(i)}) - m^{(i)} \right\}, \tag{7}$$

and applied on $v(x, z)$ to obtain the dense reconstruction $\tilde{R}_\theta(v(x, z), z)$. The dense reconstruction provides the global information of m, but is inaccurate due to the simplification of the rock-physics model. To account for the inaccuracy, we add the well log data $m(x = x_k, z)$ as the sparse sample and combine it with the dense reconstruction to composite the pseudo label:

$$\tilde{m}(x, z) = \lambda_1 \overbrace{\tilde{R}_\theta(v(x, z), z)}^{dense\ reconstruction} + \lambda_2 \overbrace{\sum_{i=1}^{k} m(x, z) * \delta(x_k)}^{sparse\ sample} \tag{8}$$

where $\delta(\cdot)$ is the delta function. λ_1 and λ_2 are the weight for dense reconstruction and sparse sample. The dense reconstruction provides the global but inaccurate information while the sparse sample provides the accurate but local information.

The end-to-end network takes the geophysical measurements, such as seismic and EM data, as the inputs and generates geophysical properties m_{pred} (see Fig. 3). With the pseudo labels $\tilde{m}$, the network g can be trained with the loss function $\mathcal{L}(m_{pred}, \tilde{m})$ to approximate the inverse mapping $f^{-1}(\cdot)$ as in Eq. 5.

In this paper, we set the velocity map as the source property v, which can be learned from the seismic data by UPFWI without labeling. Although WS-MGI is designed for m as the property without explicit governing equations, m can also be a property explicitly governed by PDEs. We choose m to be CO_2 saturation and conductivity to validate the effectiveness of this method.

4. Experiments

In this section, we apply the WS-MGI method to the Kimberlina reservoir dataset. The original geophysical properties were developed under DOE's National Risk Assessment Program (NRAP) based on a potential CO_2 storage site in the Southern San Joaquin Basin of California (Alumbaugh et al., 2021). To the best of our knowledge, it is the largest dataset for multi-physics study in the geophysics discipline. The dataset contains 780 samples. Each sample contains a set of seismic and EM data as geophysical measurements, velocity, conductivity, and CO_2 saturation maps as earth properties, and two well log records that provide CO_2 saturation and conductivity. In our experiments, 750 samples are used for training and the rest are used for validation.

Table 1. The MAE, MSE and SSIM losses with UPFWI results

Seismic Data Loss			Velocity Map Loss		
MAE	MSE	SSIM	MAE	MSE	SSIM
0.0275	0.0009	0.8909	0.0131	0.0008	0.9130

4.1. Kimberlina Data

The saturation maps and velocity maps are with the size of 59×100 ($H \times W$), where H and W are the depth and the width of the maps. The grid is 60 m in all dimensions. Two well logs are located at 2 km and 4 km. The size of the seismic data is $5 \times 1000 \times 100$ ($S \times T \times R$), where S and R are the number of sources and receivers and T is the time steps. EM data do not have a time axis, its size is $(2 \times 16 \times 100)$ ($S \times F \times R$), where F is the number of the frequencies. The examples of the geophysical measurement are given in Appendix.

4.2. UPFWI

We implement UPFWI to obtain the velocity maps. The details of the implementation are given in the Appendix. The MSE, MAE, and SSIM between the input and predicted seismic data and between the true and predicted velocity maps are listed in Table 1, which shows that the predicted velocity maps given by UPFWI are accurate.

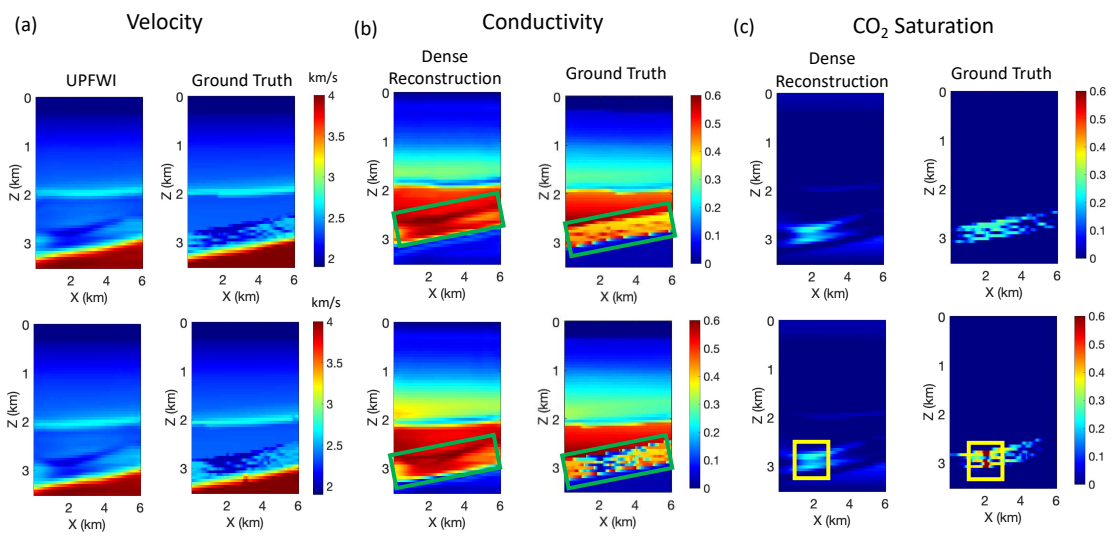

Figure 4. (a) Velocity maps given by UPFWI. (b) Conductivity dense reconstruction and true conductivity map. (c) CO_2 saturation dense reconstruction and true CO_2 saturation map.

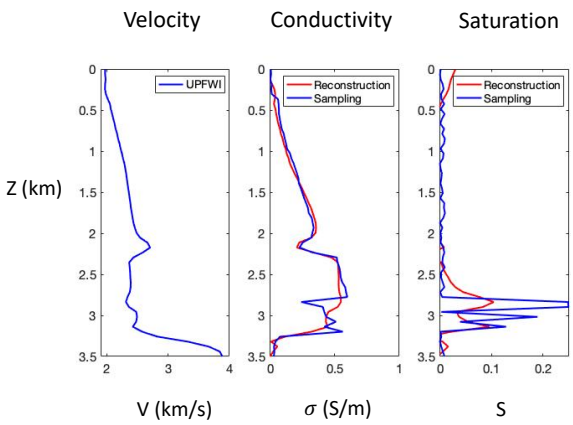

Figure 5. Examples of profiles: the velocity profile provided by UPFWI, the sparse samples provided by well logs and the dense reconstructions provided by SVR of conductivity and CO_2 saturation maps.

4.3. Workflow

Stage 1: The examples of the velocity maps provided by UPFWI are shown in Fig. 4a. The resolution of the UPFWI velocity maps is lower than the true velocity maps due to the limitation of the frequency in full waveform inversion (Schuster, 2017).

Stage 2: We use two well logs at $x = 2\ km$ and $x = 4\ km$ as the sparse samples ($\frac{1}{50}\times$full labels) and the UPFWI velocity maps (see Fig. 5) at the corresponding location in the training of SVR to predict the dense reconstructions. The predicted dense reconstructions are shown in Figs. 4b and 4c and their vertical profiles are shown in Fig. 5. We can see the dense reconstruction is inaccurate, especially the reservoir area in conductivity map (see Green boxes in Fig. 4b) and the high saturation area in CO_2 saturation map (see Yellow boxes in Fig. 4c). Then we combine the inaccurate dense reconstructions and the accurate sparse samplings to construct pseudo labels with Eq. (8). The pseudo labels are fed into an end-to-end network g to learn the mapping from the seismic and EM data to conductivity and CO_2 saturation as in Eq. (5).

4.4. Implement Details

Training Details: The input seismic and EM data are normalized into the range [-1,1]. We employ Adam optimizer with momentum parameters $\beta_1 = 0.5$ and $\beta_2 = 0.999$. The learning rate is set to be 1×10^{-4}, and it gradually decreases with the increasing number of epochs. The size of the mini-batch is set to be 10. The ℓ_1 loss function is used in the training. We implement our networks in Pytorch and train them on a Tesla V100 GPU with 50 epochs. All networks are randomly initialized.

Networks: The measurements (seismic and EM data) and the properties (conductivity and CO_2 saturation) are connected by an encoder-decoder network. The encoder with seismic data as the input has 7 convolutional layers (with stride 2 every the other layer to reduce dimension) and the encoder which uses EM data as its input has 5 convolutional layers. The decoder is composed of 4 convolutional layers expanded with nearest neighbor upsampling, followed by center-cropping of the feature map and a convolution layer

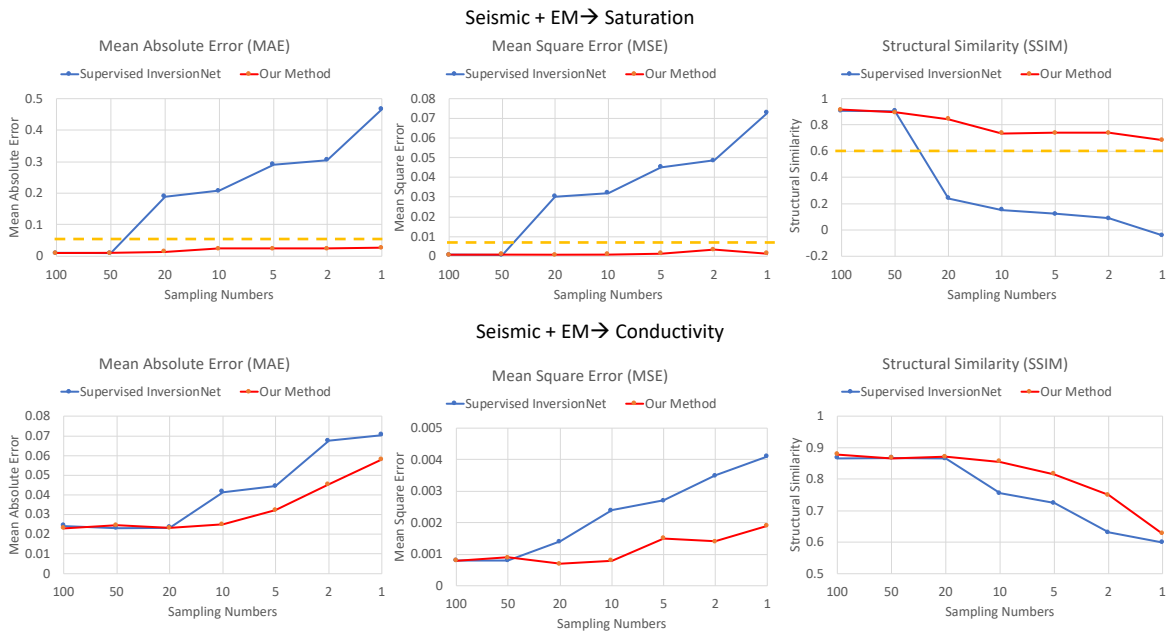

Figure 6. **Weakly Supervised Multiple Geo-physics Inversion (ours) vs. Supervised InversionNet (Wu & Lin, 2019)**. Our method achieves better performance e.g. lower Mean Absolute Error (MAE) and higher Structural Similarity (SSIM).

.

to output the property map. If both seismic and EM data are used as inputs, they are fed into two parallel encoders and concatenated in the latent spaces. The concatenated latent spaces are then fed into the decoder to give the output properties.

Evaluation Metrics: The mean-square errors (MSE), mean-absolute errors (MAE), and Structural Similarity (SSIM) are used for evaluating the conductivity and saturation results. MSE and MAE are widely used in the existing geophysical inversion methods (Araya-Polo et al., 2018; Wu & Lin, 2019). The high-level structure in the geological formation can be easily distinguished by human vision. To better align with human vision, we use SSIM as one of our evaluation metrics (Jin et al., 2021).

Comparison: As there are no existing inversion methods designed specifically for the inversion with sparse labeling, we compare our methods with the supervised InversionNet method (Wu & Lin, 2019; Zeng et al., 2021). The structure of the end-to-end network in the InversionNet is the same as our method. There are totally 100 samples, which we gradually decrease to evaluate the performance of the methods when the sampling becomes more and more sparse.

4.5. Main Results

Fig. 6 compares the results with the supervised InversionNet and our method on two scenarios:

Seismic+EM→CO_2 Saturation: In this scenario, seismic and EM data are set as the input measurement and the target property m is CO_2 saturation. The ratio between the weight λ_1 and λ_2 is set as 1. When the sampling number is less than 20 ($\frac{1}{5}\times$full labels), the performance of InversionNet quickly degrades. The MAE becomes higher than 0.2, MSE increases to 0.03, and SSIM decreases to 0.2. Our method maintains MAE less than 0.05, MSE less than 0.01, and SSIM higher than 0.6. Examples of the results are shown in Fig. 7. The saturation maps given by InversionNet contain a large amount of artifacts in the background. The results with our WS-MGI method are consistent with the ground truth. Moreover, the high saturation zone in the yellow box is inverted clearly.

Seismic+EM→Conductivity: In this scenario, seismic and EM data are the input measurements, and the target property m is conductivity. The ratio between the weight λ_1 and λ_2 is set as 10. The relationship between the conductivity and EM data is governed by the PDE. When the sampling number decreases, the performance of InversionNet decreases slower than the saturation. However, our methods still have lower MAE, lower MSE, and higher SSIM than those of InversionNet for all the sampling numbers. In Fig. 7, the thin layers in the blue boxes are reconstructed much better in our result than those obtained using InversionNet.

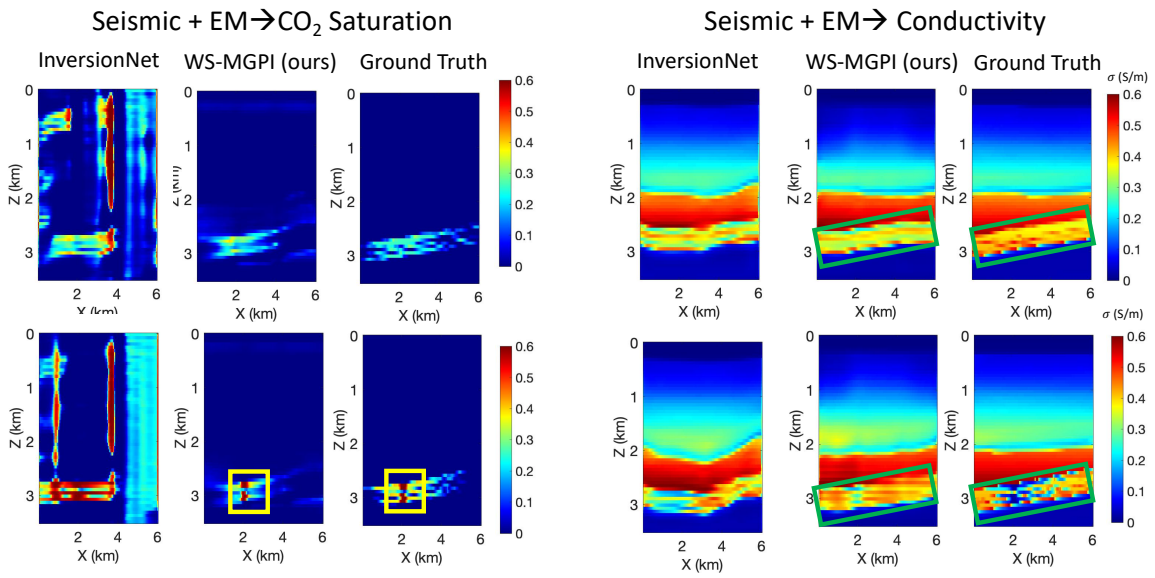

Figure 7. Comparison of InversionNet and WS-MGI (ours) on inverted CO_2 saturation and conductivity maps when sampling number equal to 2.

5. Ablation Study

In this section, we discuss different factors that affect the performance of our method. Five tests are studied below and more results are given in the Appendix.

5.1. The Inversion Scenarios

We have tested 5 different scenarios, in which conductivity and saturation are inverted from EM and seismic data. For each scenario, we compare the results with different labels (sparse sample, dense reconstruction, and pseudo label in Eq. (8)) as the training labels for the network. The inversion with sparse sampling would be the same as the supervised learning with sparse labeling. Their quantitative results are listed in Table 2 and examples of the results are given in the Appendix. For the inversion of conductivity, the sparse sample can give a reasonable result while it can only provide poor results for the inversion of CO_2 saturation. Among all the scenarios, the performance of the pseudo labels is always the best.

5.2. The Weight Ratio Selection

The selection of the weight in Eq. (8) is important in the construction of the pseudo label. We have tested our methods with different weight settings. The results are given in Table. 3. For the inversion of conductivity, the sparse sampling has a good regularization of the inversion result. It has the best results when the sparse sample has a higher weight $\lambda_1/\lambda_2 = 0.1$. For saturation, a balanced weight $\lambda_1/\lambda_2 = 1$ is the best option.

Table 2. Quantitative results with different label setting in different inversion scenarios

		MAE↓	MSE↓	SSIM↑
Seismic→Saturation	Sampling	0.1603	0.0520	0.2554
	Reconstruction	0.0271	0.0037	0.6837
	Pseudo	**0.0175**	**0.0022**	**0.7911**
EM→Saturation	Sampling	0.5318	0.1678	-0.0150
	Reconstruction	0.0229	0.0028	0.7147
	Pseudo	**0.0222**	**0.0028**	**0.7273**
{EM, Seismic}→Saturation	Sampling	0.2449	0.0771	0.1691
	Reconstruction	0.0273	0.0037	0.6844
	Pseudo	**0.0193**	**0.0034**	**0.7388**
EM→Conductivity	Sampling	0.0523	0.0031	0.7019
	Reconstruction	0.0664	0.0029	0.5858
	Pseudo	**0.0450**	**0.0015**	**0.7126**
{EM, Seismic}→Conductivity	Sampling	0.0519	0.0030	0.6921
	Reconstruction	0.0691	0.0029	0.5792
	Pseudo	**0.0452**	**0.0024**	**0.7388**

5.3. The Accuracy of Dense Reconstruction

The dense reconstruction in Eq. (8) is obtained by the Gaussian Kernel Regression from the sparse sampling in WS-MGI, and its accuracy affects the inversion results. To study the influence of the dense reconstruction on the results, we apply different Gaussian filters on the ground truth to approximate dense reconstructions of different accuracy. Table 4 shows the results with the smoothed ground truth as the dense reconstructions. With the increase of the σ value in the filter, the accuracy of the dense reconstruction decreases. As a result, the performance of the WS-MGI

Table 3. The MAE, MSE and SSIM losses with Different Weight Ratio λ_1/λ_2

	Weight Ratio λ_1/λ_2	MAE↓	MSE↓	SSIM↑
$\left\{\begin{matrix}\text{EM}\\\text{Seismic}\end{matrix}\right\}\rightarrow$Saturation	0.1	0.0251	0.0016	0.7327
	0.2	0.0242	0.0014	0.7444
	0.5	0.0243	0.0015	0.7416
	1	**0.0239**	**0.0014**	**0.7486**
	2	0.0249	0.0016	0.7182
	5	0.0246	0.0016	0.7343
	10	0.0255	0.0016	0.6980
	Weight Ratio λ_1/λ_2	MAE↓	MSE↓	SSIM↑
$\left\{\begin{matrix}\text{EM}\\\text{Seismic}\end{matrix}\right\}\rightarrow$Conductivity	0.1	**0.0452**	**0.0024**	**0.7388**
	0.2	0.0578	0.0021	0.6362
	0.5	0.0599	0.0024	0.6203
	1	0.0610	0.0024	0.6162
	2	0.0617	0.0023	0.6059
	5	0.0616	0.0024	0.6095
	10	0.0611	0.0024	0.6171

Table 4. The MAE, MSE and SSIM losses with Different Smoothed Ground Truth as Dense Reconstruction

	Gaussian Filter σ	MAE↓	MSE↓	SSIM↑
$\left\{\begin{matrix}\text{EM}\\\text{Seismic}\end{matrix}\right\}\rightarrow$Saturation	0.5	0.0075	0.0006	0.9443
	1	0.0121	0.0011	0.8778
	3	0.0151	0.0011	0.8535
	5	0.0173	0.0009	0.8412
	Gaussian Filter σ	MAE↓	MSE↓	SSIM↑
$\left\{\begin{matrix}\text{EM}\\\text{Seismic}\end{matrix}\right\}\rightarrow$Conductivity	0.5	0.0294	0.0013	0.8149
	1	0.0326	0.0326	0.8081
	3	0.0408	0.0008	0.7488
	5	0.0517	0.0013	0.6968

would also decrease.

5.4. Robustness to Noise

The geophysical measurements, seismic data, and EM data are collected in the field contain noise. To demonstrate the robustness of the proposed WS-MGI methods against noise, we impose random noise in the measurements and test WS-MGI under different signal-to-noise ratios (SNR). Table 5 shows the results of this experiment, from which it can be observed that WS-MGI with conductivity maintains competitive performance until $\mathrm{SNR} = -10\ \mathrm{dB}$ and WS-MGI with CO_2 saturation keeps good performance until $\mathrm{SNR} = 0\ \mathrm{dB}$. However, a real-world environment with a constant negative SNR is rare. WS-MGI is therefore robust to noise in typical application scenarios.

5.5. Missing Traces in the Measurements

In the geophysical field experiments, there are always traces missing in acquired measurements because of existing obstacles and economic restrictions (Wang et al., 2019). The robustness of the network with the missing traces would be crucial for practical application. We test our methodology on data with missing traces as in Table 6. The performance

Table 5. The MAE, MSE and SSIM losses with Different Noise Level

	SNR	MAE↓	MSE↓	SSIM↑
$\left\{\begin{matrix}\text{EM}\\\text{Seismic}\end{matrix}\right\}\rightarrow$Saturation	40	0.0249	0.0015	0.7317
	30	0.0251	0.0015	0.7144
	20	0.237	0.0014	0.7449
	10	0.0256	0.0019	0.7227
	0	0.0295	0.0023	0.6468
	-10	0.0310	0.0024	0.6293
	-20	0.0300	0.0024	0.6558
	-30	0.0306	0.0024	0.6462
	SNR	MAE↓	MSE↓	SSIM↑
$\left\{\begin{matrix}\text{EM}\\\text{Seismic}\end{matrix}\right\}\rightarrow$Conductivity	40	0.0471	0.0026	0.7241
	30	0.0471	0.0026	0.7243
	20	0.0469	0.0026	0.7250
	10	0.0414	0.0052	0.7798
	0	0.0412	0.0052	0.7794
	-10	0.0455	0.0064	0.7414
	-20	0.0639	0.0113	0.6389
	-30	0.1030	0.0210	0.5013

Table 6. The MAE, MSE and SSIM losses with Missing Traces in the Measurements

	Missing Traces (%)	MAE↓	MSE↓	SSIM↑
$\left\{\begin{matrix}\text{EM}\\\text{Seismic}\end{matrix}\right\}\rightarrow$Saturation	30	0.0256	0.0017	0.7257
	60	0.0267	0.0018	0.7186
	90	0.0300	0.0040	0.6935
	Missing Traces (%)	MAE↓	MSE↓	SSIM↑
$\left\{\begin{matrix}\text{EM}\\\text{Seismic}\end{matrix}\right\}\rightarrow$Conductivity	30	0.0475	0.0026	0.7178
	60	0.0552	0.0030	0.6641
	90	0.0678	0.108	0.6101

of the WS-MGI gradually decreases when the available data becomes less.

6. Conclusions

In this paper, we propose Weakly Supervised Multiple Geo-Physics Inversion (WS-MGI) which solves multi-physics inversion problem with sparse sampling. With pseudo labels built from the sparse labeling of the geophysics properties, we are able to train an end-to-end network that learns the mapping from the measurement to the geophysical property. This network enables the inversion of geophysical properties that only have an implicit relationship with the measurement. Moreover, solving the multi-physics inversion in a weakly supervised way mitigates the high cost of label collection, which is much more practical than the previously existing supervised inversion methods.

We successfully implement this method with Kimberline data on the inversion of CO_2 saturation and conductivity. Compared with the supervised inversion methods that require at least 20 samples ($\frac{1}{5}\times$full labels), WS-MGI successfully reconstructs the geological structures and CO_2 saturation with only 2 well logs as the sparse samples ($\frac{1}{50}\times$full labels).

References

Alumbaugh, D., Commer, M., Crandall, D., Gasperikova, E., Feng, S., Harbert, W., Li, Y., Lin, Y., Manthila Samarasinghe, S., and Yang, X. Development of a multi-scale synthetic data set for the testing of subsurface CO_2 storage monitoring strategies. In American Geophysical Union (AGU 2021), 2021.

Araya-Polo, M., Jennings, J., Adler, A., and Dahlke, T. Deep-learning tomography. The Leading Edge, 37(1): 58–66, 2018.

Bassiouni, Z. et al. Theory, measurement, and interpretation of well logs, volume 4. Henry L. Doherty Memorial Fund of AIME, Society of Petroleum Engineers, 1994.

Chen, Y., Feng, Z., Fu, L., AlTheyab, A., Feng, S., and Schuster, G. Multiscale reflection phase inversion with migration deconvolution. Geophysics, 85(1):R55–R73, 2020.

Commer, M. and Newman, G. A. New advances in three-dimensional controlled-source electromagnetic inversion. Geophysical Journal International, 172(2):513–535, 2008.

Ellis, D. V. and Singer, J. M. Well logging for earth scientists, volume 692. Springer, 2007.

Engquist, B. and Majda, A. Absorbing boundary conditions for numerical simulation of waves. Proceedings of the National Academy of Sciences, 74(5):1765–1766, 1977.

Feng, S. and Schuster, G. T. Transmission+ reflection anisotropic wave-equation traveltime and waveform inversion. Geophysical Prospecting, 67(2):423–442, 2019.

Feng, S., Fu, L., Feng, Z., and Schuster, G. T. Multiscale phase inversion for vertical transverse isotropic media. Geophysical Prospecting, 69(8-9):1634–1649, 2021a.

Feng, S., Lin, Y., and Wohlberg, B. Multiscale data-driven seismic full-waveform inversion with field data study. arXiv preprint arXiv:2103.04007, 2021b.

Hoversten, G. M., Gritto, R., Washbourne, J., and Daley, T. Pressure and fluid saturation prediction in a multicomponent reservoir using combined seismic and electromagnetic imaging. Geophysics, 68(5):1580–1591, 2003.

Jin, P., Zhang, X., Chen, Y., Huang, S. X., Liu, Z., and Lin, Y. Unsupervised learning of full-waveform inversion: Connecting cnn and partial differential equation in a loop. arXiv preprint arXiv:2110.07584, 2021.

Lee, D.-H. et al. Pseudo-label: The simple and efficient semi-supervised learning method for deep neural networks. In Workshop on challenges in representation learning, ICML, volume 3, pp. 896, 2013.

Lelièvre, P. G., Farquharson, C. G., and Hurich, C. A. Joint inversion of seismic traveltimes and gravity data on unstructured grids with application to mineral exploration. Geophysics, 77(1):K1–K15, 2012.

Li, Y. and Oldenburg, D. W. 3-d inversion of gravity data. Geophysics, 63(1):109–119, 1998.

Lucia, F. J., Kerans, C., and Jennings, J. W. Carbonate reservoir characterization. Journal of Petroleum Technology, 55(06):70–72, 2003.

Lukawski, M. Z., Anderson, B. J., Augustine, C., Capuano Jr, L. E., Beckers, K. F., Livesay, B., and Tester, J. W. Cost analysis of oil, gas, and geothermal well drilling. Journal of Petroleum Science and Engineering, 118:1–14, 2014.

Ma, T., Chen, P., and Zhao, J. Overview on vertical and directional drilling technologies for the exploration and exploitation of deep petroleum resources. Geomechanics and Geophysics for Geo-Energy and Geo-Resources, 2 (4):365–395, 2016.

Moczo, P., Robertsson, J. O., and Eisner, L. The finite-difference time-domain method for modeling of seismic wave propagation. Advances in geophysics, 48:421–516, 2007.

Schuster, G. T. Seismic inversion. Society of Exploration Geophysicists, 2017.

Sun, Y., Denel, B., Daril, N., Evano, L., Williamson, P., and Araya-Polo, M. Deep learning joint inversion of seismic and electromagnetic data for salt reconstruction. In SEG Technical Program Expanded Abstracts 2020, pp. 550–554. Society of Exploration Geophysicists, 2020.

Virieux, J. and Operto, S. An overview of full-waveform inversion in exploration geophysics. Geophysics, 74(6): WCC1–WCC26, 2009.

Wang, B., Zhang, N., Lu, W., and Wang, J. Deep-learning-based seismic data interpolation: A preliminary result. Geophysics, 84(1):V11–V20, 2019.

Wu, Y. and Lin, Y. Inversionnet: An efficient and accurate data-driven full waveform inversion. IEEE Transactions on Computational Imaging, 6:419–433, 2019.

Yilmaz, Ö. Seismic data analysis: Processing, inversion, and interpretation of seismic data. Society of exploration geophysicists, 2001.

Zeng, Q., Feng, S., Wohlberg, B., and Lin, Y. Inversionnet3d: Efficient and scalable learning for 3d full waveform inversion. arXiv preprint arXiv:2103.14158, 2021.

Zhdanov, M. S. Geophysical electromagnetic theory and methods. Elsevier, 2009.

Zhdanov, M. S., Fang, S., and Hursán, G. Electromagnetic inversion using quasi-linear approximation. Geophysics, 65(5):1501–1513, 2000.

Zhdanov, M. S., Jorgensen, M., and Cox, L. Advanced methods of joint inversion of multiphysics data for mineral exploration. Geosciences, 11(6):262, 2021.

A. Appendix

A.1. Unsupervised Physical-Informed Full Waveform Inversion (UPFWI)

The illustration of UPFWI is shown in Figure 8. An encoder-decoder structure is connected with the forward modeling of the seismic data to model the mapping from seismic data $\mathbf{p} \in \mathbb{R}^{S\times T\times R}$ to velocity map $\mathbf{v} \in \mathbb{R}^{H\times W}$. It is trained in an unsupervised way by minimizing $\mathcal{L}_{seis}$:

$$\mathcal{L}_{seis} = \frac{1}{2}\sum ||f_{seis}(\mathbf{v}) - \mathbf{p}||, \tag{9}$$

where $\mathbf{p}$ is the input seismic data, $\mathbf{v}$ is the predicted velocity map, f_{seis} is the forward modeling operator is governed by the wave equation using a finite-difference method (Moczo et al., 2007).

Training Details: The seismic data from different sources are aligned in different channels and normalized into a range of [-1,1] as the input of neural network. We employ Adam optimizer with momentum parameters $\beta_1 = 0.5$ and $\beta_2 = 0.999$. The learning rate is set to be 3×10^{-5} and it gradually decreases with increasing epochs. The size of the mini-batch is set to be 10. The ℓ_2 loss function is used during training. We implement UPFWI in Pytorch and train the networks on a Tesla V100 GPU with 250 epochs.

Networks: The encoder in UPFWI is primarily built with 7 convolutional layers (with a stride of 2 every the other layer to reduce dimensions), which extract the high-dimensional features from the seismic data. The decoder projects the extracted features into velocity maps through 4 convolutional layers with intermediate nearest neighbor upsampling. Finally, we center-crop the feature maps and apply a convolution layer to output the velocity map.

A.2. Geophysical Measurements

There are 5 seismic sources placed evenly on the 2D spatial grid over the surface with a shot interval of 1.2 km. Seismic data are simulated using the finite-difference method (Moczo et al., 2007) with absorbing boundary conditions (Engquist & Majda, 1977). EM data are simulated by finite-difference method (Commer & Newman, 2008) with two sources location at $x = 2.5\ km$, $z = 3.025\ km$ and $x = 4.5\ km$, $z = 2.5\ km$ with 8 source frequencies from 0.1 to 8.0 Hz. Both the seismic and EM data are collected by 100 receivers uniformly distributed over the 2D earth surface with a receiver interval of 60 m. Each sensor captures seismic vibration signals as time-series data of length 1,000 with a time spacing of 0.005 s and EM signals contains a real part and an imaginary part with each source frequency. The examples of geophysical measurements are listed in Fig. 9.

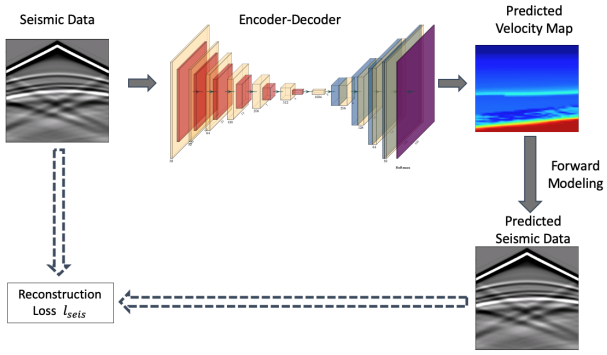

Figure 8. Schematic illustration of UPFWI, where trains an encoder-decoder to learn the mapping from seismic data to velocity maps.

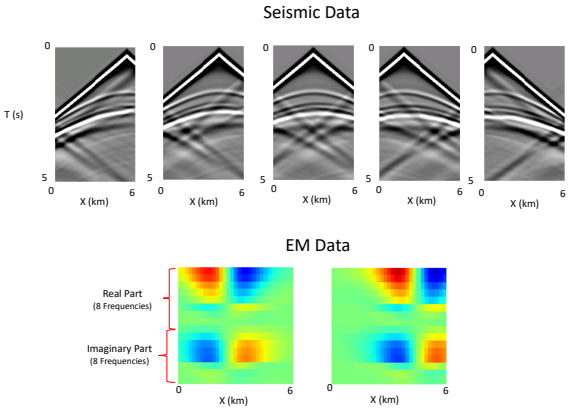

Figure 9. Examples of seismic and EM data.

A.3. Quantitative Results

Table 7 and 8 show the quantitative results corresponding to two scenarios (Seismic+EM→CO_2 saturation and Seismic+EM→Conductivity) in Fig. 6. Our WS-MGI method outperforms the InversionNet for all the cases.

Table 7. Comparison of WS-MGI (Ours) and InversionNet: the MAE, MSE and SSIM losses with Different Number of Sampling Labels (EM+seismic→Saturation)

	Sampling Labels Numbers	MAE↓	MSE↓	SSIM↑
WS-MGI (Ours)	100	0.0104	0.0008	0.9170
	50	0.0108	0.0009	0.8963
	20	0.015	0.0008	0.846
$\left\{\begin{matrix}\text{EM}\\ \text{Seismic}\end{matrix}\right\}\rightarrow\text{Saturation}$	10	0.0243	0.0009	0.7363
	5	0.0239	0.0013	0.7388
	2	0.0246	0.0034	0.7389
	1	0.0273	0.0015	0.6844
	Sampling Labels Numbers	MAE↓	MSE↓	SSIM↑
InversionNet	100	0.0104	0.0008	0.9078
	50	0.0102	0.0007	0.9066
	20	0.1901	0.0303	0.2422
$\left\{\begin{matrix}\text{EM}\\ \text{Seismic}\end{matrix}\right\}\rightarrow\text{Saturation}$	10	0.2083	0.0321	0.154
	5	0.2916	0.0452	0.1228
	2	0.306	0.0486	0.0885
	1	0.4661	0.0727	-0.0411

Table 8. Comparison of WS-MGI (Ours) and InversionNet: the MAE, MSE and SSIM losses with Different Number of Sampling Labels (EM+seismic→Conductivity)

	Sampling Labels Numbers	MAE↓	MSE↓	SSIM↑
WS-MGI (Ours)	100	0.023	0.0008	0.878
	50	0.0246	0.0009	0.8664
	20	0.0231	0.0007	0.8701
$\left\{\begin{matrix}\text{EM}\\ \text{Seismic}\end{matrix}\right\}\rightarrow\text{Conductivity}$	10	0.0249	0.008	0.8553
	5	0.0323	0.0015	0.816
	2	0.0452	0.0014	0.7486
	1	0.058	0.0019	0.6266
	Sampling Labels Numbers	MAE↓	MSE↓	SSIM↑
InversionNet	100	0.0242	0.0008	0.8658
	50	0.0231	0.0008	0.8669
	20	0.0234	0.0014	0.8657
$\left\{\begin{matrix}\text{EM}\\ \text{Seismic}\end{matrix}\right\}\rightarrow\text{Conductivity}$	10	0.0414	0.0024	0.7546
	5	0.0445	0.0027	0.7245
	2	0.0674	0.0035	0.631
	1	0.0703	0.0041	0.599

A.4. Results with Different Inversion Scenarios

We have studied 5 different scenarios from seismic and EM data to CO_2 saturation and conductivity in the ablation study. Examples of the results are listed in Fig. 10 and 11. For the inversion of CO_2 saturation, there is no constraint on the background when we only use the sparse sampling as the labels. There are lots of artifacts in the background, especially the input data is EM data only since the size of the EM data is much smaller than the seismic data. For the inversion of conductivity, the artifacts in the background are eliminated because of the constraint from the PDE.

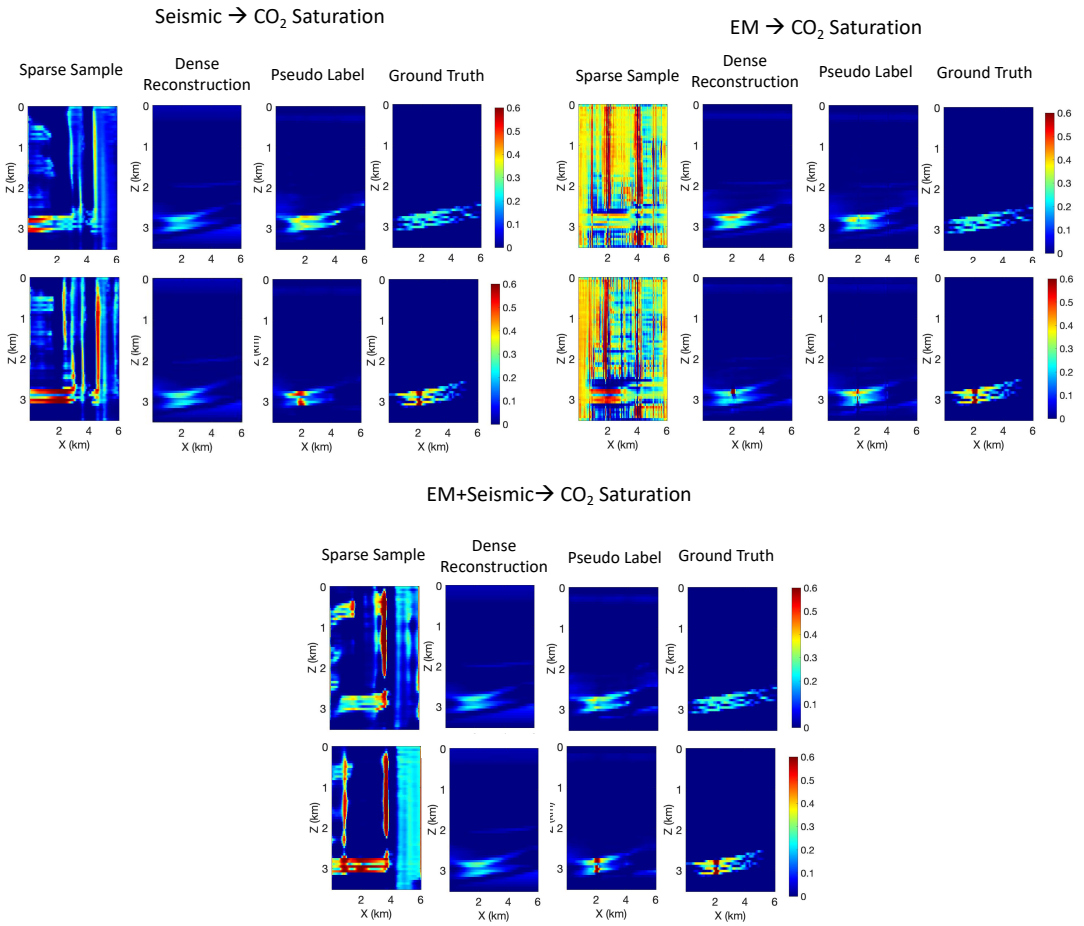

Figure 10. The comparison of inverted CO_2 saturation maps with different labels (sparse sample only, dense reconstruction only and pseudo labels) and the ground truth from different scenarios.

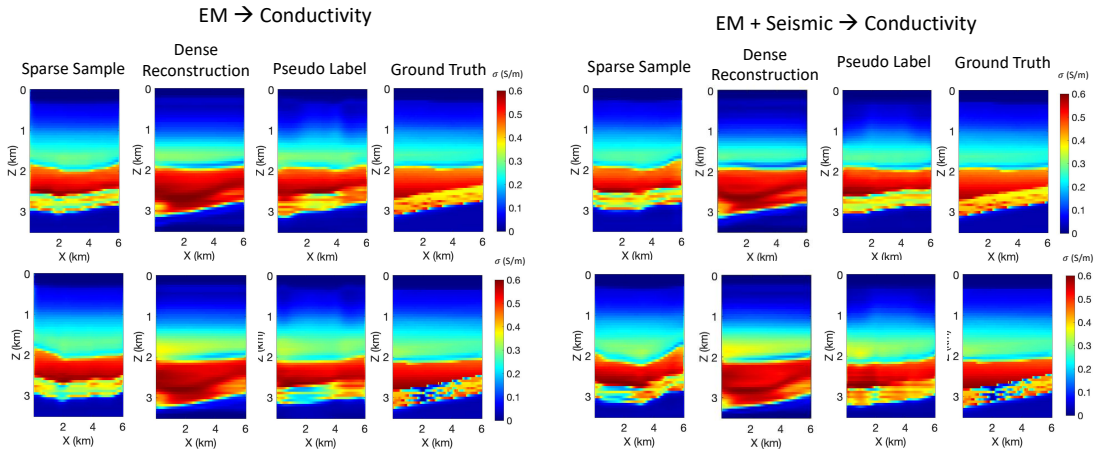

Figure 11. The comparison of inverted conductivity maps with different labels (sparse sample only, dense reconstruction only and pseudo labels) and the ground truth from different scenarios.